1 **Variational regional inverse modeling of reactive species emissions with PYVAR-CHIMERE**

2 Audrey Fortems-Cheiney[1], Isabelle Pison[1], Gaelle Dufour[2], Grégoire Broquet[1], Antoine Berchet[1],

3 Elise Potier[1], Adriana Coman[2], Guillaume Siour[2], and Lorenzo Costantino[2]

5 [1]Laboratoire des Sciences du Climat et de l'Environnement, LSCE-IPSL (CEA-CNRS-UVSQ),

6 Université Paris-Saclay, 91191 Gif-sur-Yvette, France.

7 [2]Laboratoire Interuniversitaire des Systèmes Atmosphériques, UMR CNRS 7583, Université Paris

8 Est Créteil et Université Paris Diderot, Institut Pierre Simon Laplace, Créteil, France.

10 **Abstract**

11 Up-to-date and accurate emission inventories for air pollutants are essential for understanding their

12 role in the formation of tropospheric ozone and particulate matter at various temporal scales, for

13 anticipating pollution peaks and for identifying the key drivers that could help mitigate their

14 emissions. This paper describes the Bayesian variational inverse system PYVAR-CHIMERE, which

15 is adapted to the inversion of reactive species. Complementarily with bottom-up inventories, this

16 system aims at updating and improving the knowledge on the high spatio-temporal variability of

17 emissions of air pollutants and their precursors. The system is designed to use any type of

18 observations, such as satellite observations or surface stations. The potential of PYVAR-CHIMERE

19 is illustrated with one-day inversions of CO and NO_2 emissions in Europe, using the MOPITT and

20 OMI satellite observations (for CO and for NO2, respectively).

22 **1. Introduction**

23 The degradation of air quality is a worldwide environmental problem: 91% of the world's population

24 have breathed polluted air in 2016 according to the World Health Organization (WHO), resulting in

25 4.2 millions of premature deaths every year [WHO, 2016]. The recent study of Lelieveld et al. [2019]

26 even suggests that the health impacts attributable to outdoor air pollution are substantially higher than

27 previously assumed (with 790,000 premature deaths in the 28 countries of the European Union against

28 the previously estimated 500,000 [EEA, 2018]). The main regulated primary (i.e. directly emitted in

29 the atmosphere) anthropogenic air pollutants are carbon monoxide (CO), nitrogen oxides (NO_x

30 $=NO+NO_2$), sulfur dioxide (SO_2), ammonia (NH_3), volatile organic compounds (VOCs)), and

31 primary particles. These primary gaseous air pollutants are precursors of secondary (i.e. produced in

32 the atmosphere through chemical reactions) pollutants such as ozone (O_3) and Particulate Matter

33 (PM), which are also threatening to both human health and ecosystems. Monitoring concentrations

34 and quantifying emissions are still challenging and limit our capability to forecast air quality to warn

35 population and to assess i) the exposure of population to air pollution and ii) the efficiency of

36 mitigation policies.

37

38 Bottom-up (BU) inventories are built in the framework of air quality policies such as The Convention
39 on Long-Range Transboundary Air Pollution (LRTAP) for air pollutants. Based on national annual
40 inventories, research institutes compile gridded global or regional, monthly inventories (mainly for
41 the US, Europe and China) with a high spatial resolution (currently regional or city scale inventories
42 are typically finer than $0.1°x0.1°$). These inventories are constructed by combining available
43 (economic) statistics data, from different detailed activity sectors, with the most appropriate emission
44 factors (defined as the average emission rate of a given species for a given source or process, relative
45 to the unit of activity). It is important to note that the activity data (often statistical data) has an
46 inherent uncertainty and its reliability may vary between countries or regions. In addition, the
47 emission factors bear large uncertainties in their quantification [Kuenen et al., 2014; EMEP/EEA,
48 2016; Kurokawa et al., 2013]. Moreover, these inventories are often provided at the annual or monthly
49 scale with typical temporal profiles to build the weekly, daily and hourly variability of the emissions.
50 The combination of uncertain activity data, emission factors and emission timing can be a large source
51 of uncertainties, if not errors, for forecasting or analyzing air quality [Menut et al., 2012]. Finally,
52 since updating the inventories and gathering the required data for a given year is costly in time,
53 manpower and money, only a few institutes have offered estimates of the gaseous pollutants for each
54 year since 2011 (i.e, EMEP updated until the year 2017, MEIC updated until the year 2017 to our
55 knowledge). Nevertheless, using knowledge from inventories and air quality modelling, emissions
56 could have been mitigated. For example, from 2010 to nowadays, emissions in various countries have
57 been modified and/or regional trends have been reversed (e.g., the decrease of NO_x emissions over
58 China since 2011 [de Foy et al., 2016]), leading to significant changes in the atmospheric
59 composition. Consequently, the knowledge of precise and updated budgets, together with seasonal,
60 monthly, weekly and daily variations of gaseous pollutants driven, amongst other processes, by the
61 emissions are essential for understanding their role in the formation of tropospheric ozone and PMs
62 at various temporal scales, for anticipating pollution peaks and for identifying the key drivers that
63 could help mitigate these emissions.

64

65 In this context, complementary methods have been developed for estimating emissions using
66 atmospheric observations. They operate in synergy between a chemistry-transport model (CTM) -
67 which links the emissions to the atmospheric concentrations-, atmospheric observations of the species
68 of interest, and statistical inversion techniques. A number of studies using inverse modeling were first
69 carried out for long-lived species such as greenhouses gases (GHGs) (e.g., carbon dioxide CO_2 or
70 methane CH_4) at the global or continental scales [Hein et al., 1997; Bousquet et al. 1999], using
71 surface measurements. Later, following the development of monitoring station networks, the progress

72   of computing power, and the use of inversion techniques more appropriate to non-linear problems,

73   these methods were applied to shorter-lived molecules such as CO. For these various applications

74   (e.g., for CO_2, CH_4, CO), the quantification of sources was solved at the resolution of large regions

75   [Pétron et al., 2002]. Finally, the growing availability and reliability of observations since the early

76   2000s (in-situ surface data, remote sensing data such as satellite data), the improvement of the global

77   CTMs, of the computational capacities and of the inversion techniques have increased the achievable

78   resolution of global inversions, up to the global transport model grid cells, i.e. typically with a spatial

79   resolution of several hundreds of square kilometers [Stavrakou and Muller, 2006; Pison et al., 2009;

80   Fortems-Cheiney et al., 2011; Hooghiemstra et al., 2012; Yin et al., 2015; Miyazaki et al., 2017,

81   Zheng et al., 2019].

82

83   Today, the scientific and societal issues require an up-to-date quantification of pollutant emissions at

84   a higher spatial resolution than the global one and imply to widely use regional inverse systems.

85   However, although they are suited to reactive species such as CO, NO_x, and their very large spatial

86   and temporal variability, they have hardly been used to quantify pollutant emissions. Some studies

87   inferred NO_x [Pison et al., 2007; Tang et al., 2013] and VOC emissions [Koohkan et al., 2013] from

88   surface measurements. Konovalov et al. [2006, 2008, 2010], Mijling et al. [2012, 2013], Van der A.

89   [2008], Lin et al. [2012] and Ding et al. [2017] have also shown that satellite observations are a

90   suitable source of information to constrain the emissions of NO_x. These regional inversions using

91   satellite observations were often based on Kalman Filter (KF) schemes [Mijling et al., 2012, 2013;

92   Van der A., 2008; Lin et al., 2012; Ding et al., 2017]. However, these inversion problems may be

93   impacted by the non-linearity of atmospheric chemistry, for which variational methods are more

94   suitable than KFs by design.

95

96   Here, we present the Bayesian variational inverse system PYVAR-CHIMERE, that has reached a

97   good level of maturity (robustness of calculations, clarity, portability, modularity of the code) and

98   that is adapted to reactive species such as CO and NO_2. This adaptation for reactive species takes

99   advantage of the previous developments for the quantification of fluxes of long-lived GHG species

100   such as CO_2 [Broquet et al., 2011] and CH_4 [Pison et al., 2018] at the regional to the local scales,

101   paving the way for monitoring anthropogenic emissions at high spatial resolutions. The PYVAR-

102   CHIMERE inverse modeling system is based on the Bayesian variational assimilation code PYVAR

103   [Chevallier et al. 2005] and on the regional state-of-the-art CTM CHIMERE, dedicated to the study

104   of regional atmospheric pollution events [Menut et al., 2013, Mailler et al., 2017]. Variational

105   techniques require the adjoint of the model to compute the sensitivity of simulated atmospheric

106   concentrations to corrections of the fluxes. CHIMERE is one of the few CTMs all over the world

107   possessing its adjoint code (e.g., for global models: IMAGES [Stavrakou and Muller, 2006], TM5

108   [Krol et al., 2008], GELKA [Belikov et al., 2016] and LMDz [Chevallier et al., 2005; Pison et al.,

109   2009] ; for limited-area models: CMAQ [Hakami et al., 2007], EURAD-IM [Elbern et al., 2007],

110   RAMS/CTM-4DVAR [Yumimoto et Uno, 2006]). Originally, the sequential adjoint code was

111   developed at LMD [Menut et al., 2000; Menut et al., 2003]. Then, it has been further developed and

112   parallelized at LISA [Pison et al., 2007] and LSCE (see Section 3).

113

114   The principle of variational atmospheric inversion and the configuration of PYVAR-CHIMERE are

115   described in Section 2 and in Section 3, respectively. Details about the forward and adjoint codes are

116   also given. Then, the potential of PYVAR-CHIMERE is illustrated in Section 4 with the optimization

117   of European CO and NO_2 emissions, constrained by observations from the Measurement of Pollution

118   in the Troposphere (MOPITT) instrument and from the Ozone Monitoring Instrument (OMI).

119

120   **2. Principle of Bayesian variational atmospheric inversion**

121   The Bayesian variational atmospheric inversion method adjusts a set of control parameters in input

122   of the CTM, including parameters related to the emissions whose estimate is the primary target of the

123   inversion. The control parameters may also include initial and boundary conditions for the

124   atmospheric species of interest in the CTM. The adjustments are applied to prior values, usually taken,

125   for the emissions, from pre-existing BU inventories. The principle is to minimize, on the one hand,

126   the departures from the prior estimates of the control parameters (term J_b in Equation 1), which are

127   weighted by the uncertainties in these estimates (called hereafter "prior uncertainties"), and, on the

128   other hand, the differences between simulated and observed concentrations (term J_o in Equation 1),

129   which are weighted by all other sources of uncertainties explaining these differences (called hereafter

130   all together "observation errors"). In statistical terms, the inversion searches for the most probable

131   estimate of the control parameters given their prior estimates, the observations, the CTM and the

132   associated uncertainties. The solution, which will be called posterior estimate in the following, is

133   found by the iterative minimization of a cost function J [Talagrand et al., 1997], defined as:

$$J(x) = \underbrace{(x - x_b)^T B^{-1} (x - x_b)}_{J_b} + \underbrace{(H(x) - y)^T R^{-1} (H(x) - y)}_{J_o}$$

134   (Eq. 1)

135

136   The control vector **x** contains the variables to be optimized during the inversion process (surface

137   fluxes but also initial or boundary conditions for example, see Section 3.3). H is the non-linear

138   observation operator that projects the state vector **x** onto the observation space. In most of the

139   variational atmospheric inversion cases (such as those described in Section 4), the observation

140   operator includes the CTM and an interpolation or an extraction and averaging of the simulated fields

141 (see Section 3.4). The observations in **y** could be surface measurements and/or remote sensing data

142 such as satellite data. The prior uncertainties and the observation errors are assumed to be centered

143 and to have a Gaussian distribution. Consequently, the prior uncertainties are characterized by their

144 covariance matrix **B** and the observation errors are characterized by their covariance matrix **R.** By

145 definition, the observation errors combine errors in both the data and the observation operator, in

146 particular the combination of measurement errors and errors in the conversion of satellite

147 measurement into concentration data, errors from the CTM, representativity errors due to the

148 comparison between point measurements and gridded models or due to the representation of the

149 fluxes as gridded maps at a given spatial resolution, and aggregation errors associated with the control

150 of emissions at a given spatial and/or temporal resolution that is different from (usually coarser than)

151 that of the CTM.

152

153 For non-linear problems, as it is the case with reactive species, the minimum of J may be reached

154 iteratively with a descent algorithm. In this case, the iterative minimization of J is based on a gradient

155 method. J is calculated with the forward observation operator (including the CTM) and its gradient

156 relative to the control parameters **x** is provided by the adjoint operator (including the adjoint of the

157 CTM):

158 $$GradJ(x) = B^{-1}(x - x_b) + H^T R^{-1}(Hx - y) \quad (Eq.2)$$

159 As shown in Figure 1, the minimization algorithm repeats the forward-adjoint cycle to seek an optimal

160 solution for the control parameters.

161

162 In PYVAR-CHIMERE, we use the M1QN3 limited memory quasi-Newton minimization algorithm

163 [Gilbert and Lemaréchal, 1989]. As most quasi-Newtonian methods, it requires an initial

164 regularization of **x**, the vector to be optimized, for better efficiency. We adopt the most generally used

165 regularization, made by optimizing $\chi = \mathbf{B}^{1/2}(\mathbf{x} - \mathbf{x_b})$ instead of **x**. Although more optimal regularizations

166 can be chosen, the minimization with χ is preferred for its simplifying the equation to solve. This

167 transformation translates in Equation 2 as follows: $GradJ\chi = \chi + \mathbf{B}^{1/2}H^*(\mathbf{R}^{-1}(H(\mathbf{x}) - \mathbf{y}))$. The criterion

168 for stopping the algorithm is based on a threshold set on the ratio between the final and initial gradient

169 norms or on the maximum number of iterations to perform. Due to the non-linearity of the problem,

170 the minimization may reach only a local minimum.

171

172 Finally, the calculation of the posterior uncertainty is challenging in a variational inverse system.

173 Even though the analysis error covariance matrix can be explicitly written in various analytical forms,

174 it requires the inversion of matrices that are too large to invert given the current computational

175 resources in our variational approach. As a trade-off between computing resources and

176 comprehensiveness, the analysis error may be evaluated by an approach based on the spread of

177 sensitivity tests (e.g., as in [Fortems-Cheiney et al., [2012]). It can also be estimated through a Monte

178 Carlo Ensemble [Chevallier et al., 2007], implemented in PYVAR.

179
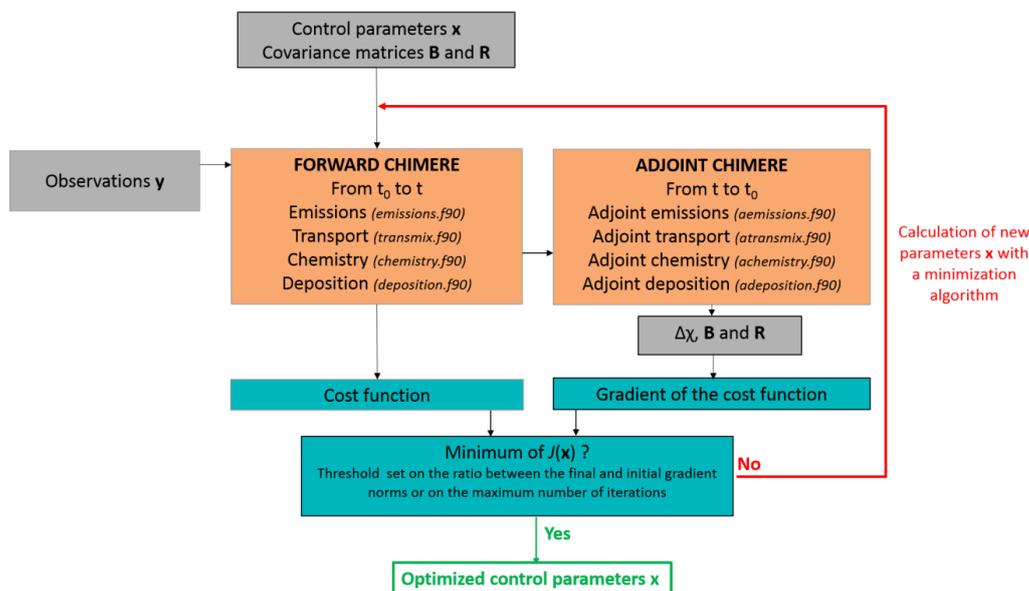
Figure 1. *Simplified scheme of the iterative minimization in PYVAR-CHIMERE. PYVAR, CHIMERE*
180
181
182 *and text sources are respectively displayed in blue, in orange and in grey.*

183

184 **3. The PYVAR-CHIMERE configuration**

185 **3.1. PYVAR adapted to CHIMERE**

186 The PYVAR-CHIMERE inverse modeling system is based on the Bayesian variational assimilation

187 code PYVAR [Chevallier et al. 2005] and on the previous inversion system based on CHIMERE

188 [Pison et al., 2007]. PYVAR is an ensemble of Python scripts, which deals with preparing the vectors

189 and the matrices for the inversion, driving the required Fortran codes of the transport model and

190 computes the minimization of the cost function to solve the inversion. Previously used for global

191 inversions with the LMDz model (e.g., Pison et al., 2009; Chevallier et al., 2010; Fortems-Cheiney

192 et al., 2011; Yin et al., 2015; Locatelli et al., 2015; Zheng et al., 2019), PYVAR has been adapted to

193 the state-of-the-art CHIMERE regional CTM. Including the elements of the previous inversion

194 system built around CHIMERE (coded in Fortran90) [Pison et al., 2007] in PYVAR (coded in Python,

195 see Section 3.5) lead to an up-to-date, more flexible and more robust system.

196

197 **3.2. Development of the adjoint of CHIMERE**

198 To compute the sensitivity of simulated atmospheric concentrations to corrections to the fluxes, the

199 adjoint of CHIMERE has been developed. Originally, the sequential adjoint was coded at LISA

200 [Menut et al., 2000; Menut et al., 2003; Pison et al., 2007]. Then, it has been parallelized and further
201 developed at LSCE and LISA, together with its tangent-linear (TL) code. The adjoint has been coded
202 by hand line by line, following the principles formulated by Talagrand [1997]. It contains exactly the
203 same processes as the CHIMERE forward model. PYVAR-CHIMERE is currently operational for
204 the full module of gaseous chemistry. As a compromise between the robustness of the method for
205 reactive species, the time required coding the adjoint and the computational cost with a full chemical
206 scheme, the aerosols modules of CHIMERE have not been included in the adjoint of CHIMERE yet
207 and are therefore not available in PYVAR-CHIMERE.

208

209 It should also be noted that other minor changes against the CHIMERE 2013 version [Menut et al.,
210 2013] have been implemented, including:
211   • For the geometry, the possibility of polar domains and the use of the coordinates of the corners
212 of the cells instead of only the centers
213   • For the transport, the non-uniform Van Leer transport scheme on the horizontal,
214   • For chemistry, various switches have been added to avoid going into the chemistry, deposition
215 and wet deposition routines when no species requires them (e.g. no chemistry for methane at a
216 regional scale).
217 It should be noted that the development and maintenance of the adjoint means that the version used
218 is   necessarily   one   or   two   versions   behind   the   distributed   CHIMERE   version
219 (http://www.lmd.polytechnique.fr/chimere/).

220

221 As an example, Figure 2 presents a simplified scheme of how PYVAR scripts are used to drive this
222 version of CHIMERE for forward simulations and inversions using satellite observations. A mode is
223 also available to test the adjoint: it runs the TL code.

224
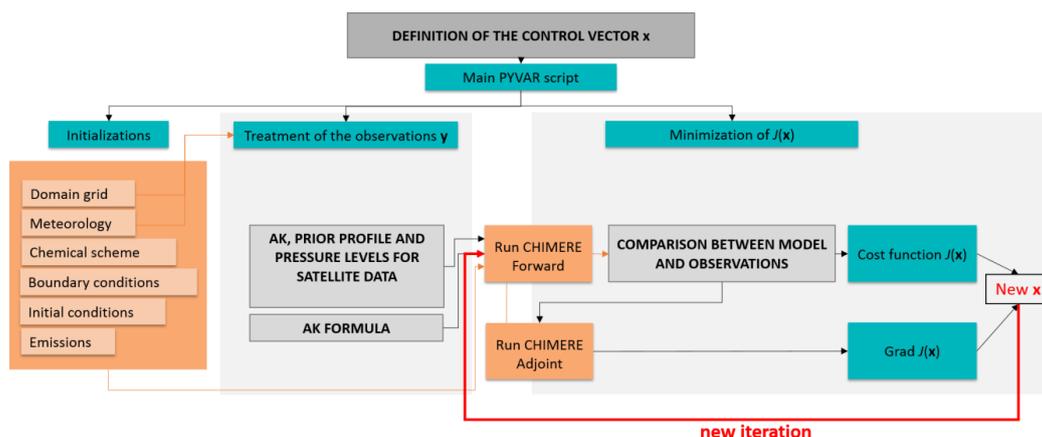
225

226 **Figure 2.** *Simplified scheme of how PYVAR scripts are used to drive CHIMERE for an inversion*

227 *using satellite observations. PYVAR, CHIMERE and text sources are respectively displayed in blue,*

228 *in orange and in grey. Note that the term AK refers to Averaging Kernel as seen in Section 3.4.*

229

230 **3.3. Definition of the control vector**

231 The control vector is specified by the user in a text file. This file is formatted following Figure 3. The

232 inputs to constrain could be fluxes, initial concentrations, boundary conditions at the top or boundary

233 conditions on the four lateral sides. The spatial resolution of the inversion could be the grid-cell

234 resolution or one whole encompassing region. A choice of simple but efficient ways of building the

235 covariance matrix **B** are implemented in PYVAR-CHIMERE. The user has only to choose:

236 - the **B** variance coefficient, to indicate how to get the variances for these components,

237 - Correlation lengths L through time and space to define the correlations. For example, the following

238 formula is used to construct the distance correlation r between two fluxes x_i and x_j: $r(x_i, x_j) =$

239 $exp\left(\frac{-d(x_i,x_j)}{L}\right)$

240 where r is the correlation between the fluxes x_i and x_j, d is the distance between these two fluxes in

241 kilometers.

Constrained species	Input to constrain	Correction type	Spatial resolution	Temporal resolution (in hours)	B variance coefficient	Time correlations in B (in hours)	Decorrelation length on land (in km)	Decorrelation length on sea (in km)
CO	Fluxes Initial conditions Boundary conditions	added	At the CHIMERE grid-cell resolution of 0.5°x0.5°	24	100 pc 10 pc 10 pc	-	-	-
NO$_2$	Fluxes Initial conditions Boundary conditions	added	At the CHIMERE grid-cell resolution of 0.5°x0.5°	24	100 pc 10 pc 10 pc	-	-	-

242
243 **Figure 3**. *Definition of the control vector and example for the illustration of Section 4.*

244 **3.4 Equivalents of the observations**

245 The individual data given as constraints in the system are first formatted into a text file described in

246 Figure 4. During forward simulations, the equivalents of the components of **y** (i.e, the equivalents of

247 the individual data) are calculated by PYVAR-CHIMERE. It includes the CTM and an interpolation

248 (see below the vertical interpolation from the model's grid to the satellite levels) or an extraction and

249 averaging (e.g. extracting the grid cell matching the geographical coordinates of a surface station and

250 averaging over one hour). As a compromise between technical issues such as the time required for

251 reading/writing files, the observation operator *H* that generates the equivalent of the observations by

252   the model (i.e. $H(\mathbf{x})$) has been so far partly embedded in the code of CHIMERE. It makes it easier to

253   use finer time intervals than available in the usual hourly outputs of CHIMERE to compute the

254   required information (e.g., within the finer CTM physical time steps).
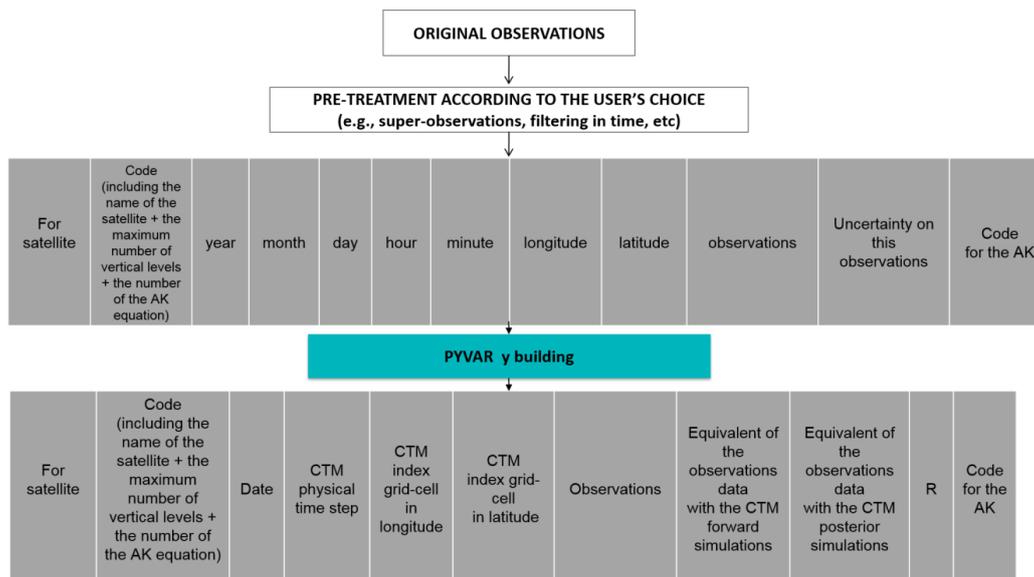
255

256   **Figure 4**. *Simplified scheme of how PYVAR scripts prepares the **y** observations, using satellite data.*

257   *PYVAR, and text sources are respectively displayed in blue and in grey.*

258

259   To make comparisons between simulations and satellite observations, the simulated vertical profiles

260   are first interpolated on the satellite's levels (with a vertical interpolation on pressure levels). Then,

261   the averaging kernels (AKs), when available, are applied to represent the vertical sensitivity of the

262   satellite retrieval. Two types of formula, depending on the satellite observations used, have been

263   detailed in PYVAR-CHIMERE for the use of AKs: $C_m = AK.C_{m(o)}$ (e.g., used by the satellite

264   instrument OMI, see Section 4.3) or $C_m = x_a + AK(C_{m(o)} - x_a)$ where $\mathbf{C_m}$ is the modeled column,

265   AK contains the averaging kernels, x_a is the prior profile (provided together with the AKs when

266   relevant) and $C_{m(o)}$ is the vertical distribution of the original model partial columns interpolated to the

267   pressure grid of the averaging kernels.

268

269   **3.5. Numerical language**

270   The PYVAR code is in Python 2.7, the CHIMERE CTM is coded in Fortran90. The CTM requires

271   several numerical tools, compilers and libraries. The CTM was developed and tested using the

272   software versions as described in Table 1.

273

		URL	Version
Software	Python	https://www.python.org/downloads/	2.7
	Fortran compiler ifort	https://software.intel.com/en-us/fortran-compilers	Composer-xe-2013.2.146
Libraries or packages	UnidataNetCDF	https://www.unidata.ucar.edu/	3
	Open MPI	https://www.open-mpi.org/	1.10.5
	GRIB_API	https://confluence.ecmwf.int/display/GRIB/Releases	1.14
	nco	http://nco.sourceforge.net/#Source	4.6.3

274 **Table 1**. *URL adresses for the development and the use of the PYVAR-CHIMERE system and its*
275 *modules.*

276
277 PYVAR-CHIMERE's computation time for one node of 10 CPUs is about 3h for 1 day of inversion
278 (with ~10 iterations) for the European domain size of 101 (longitude) x 85 (latitude) x 17 (vertical
279 levels) used in Section 4. It is also important to note that an integration of CHIMERE's adjoint is
280 about three times longer than a CHIMERE forward simulation. The model parallelism results from a
281 Cartesian division of the main geographical domain into several sub-domains, each one being
282 processed by a worker process. To configure the parallel sub-domains, the user has to specify two
283 parameters in the model parameter file: the number of sub-domains for the zonal and meridional
284 directions. The total number of CPUs used is therefore the product of these two numbers plus one for
285 the master process.

286
287 **4. Potential of PYVAR-CHIMERE for the inversion of CO and NO_2 emissions**
288 The potential of the PYVAR-CHIMERE system to invert emissions of reactive species is illustrated
289 with the inversion of the emissions of CO and NO_2 over Europe. We present results for 1-day
290 inversions. We select two different days, respectively for CO and NO_2: the 7th March 2015 and the
291 19th February 2015. These particular days have been chosen as they present a typical number of super-
292 observations (with respectively, 1587 and 3330) during winter, when the prior emissions are high.

293
294   **4.1. Set-up**
295 For both examples, CHIMERE is run over a 0.5°×0.5° regular grid (about 50x50km^2) and 17 vertical
296 layers, from the surface to 200hPa (about 12km), with 8 layers within the first two kilometers. The
297 domain includes 101 (longitude) x 85 (latitude) grid-cells (15.5°W-35°E; 31.5°N-74°N, see Figure
298 5). Meteorological fields are provided by ECMWF meteorological forecast [Owens and Hewson,
299 2018]. The chemical scheme used in PYVAR-CHIMERE is MELCHIOR-2, with more than 100
300 reactions [Derognat et al., 2003], including 22 for inorganic chemistry.

4.1.1. Control vector **x**

All the information required by the inverse system to run the inversion for CO or NO_2 emissions are listed in Table 1. The control vector **x** has 17542 components:

- the CO or NO_2 emissions at a 1- day and at a 0.5° ×0.5° (longitude, latitude) resolutions i.e. 1 day times 101x85 grid cells = 8585 components in **x** for each one-day-long inversion
- the CO or NO_2 3D initial conditions at a 0.5° ×0.5° (longitude, latitude) resolution i.e. 8585 components in **x**
- the CO or NO_2 boundary conditions at a 1- day and at a 0.5° ×0.5° (longitude, latitude) resolutions i.e. 2x101 + 2x85=372 components in **x**

The prior anthropogenic emissions for CO and NOx emissions come from the TNO inventory [Dellaert et al., 2018]. The prior anthropogenic emissions for VOCs come from the EMEP inventory. Climatological values from the LMDZ-INCA global model [Szopa et al., 2008] are used to prescribe concentrations at the lateral and top boundaries and the initial atmospheric composition in the domain.

4.1.2. Observations **y**

The observational constraints for CO emissions come from the MOPITT instrument. It has been flown onboard the NASA EOS-Terra satellite, on a low sun-synchronous orbit that crosses the equator at 10:30 and 22:30 LST. The spatial resolution of its observations is about 22x22 km^2 at nadir. It has been operated nearly continuously since March 2000. MOPITT CO products are available in three variants: thermal-infrared TIR only, near-infrared NIR only and the multispectral TIR-NIR product, all containing total columns and retrieved profiles (expressed on a ten-level grid from the surface to 100 hPa). We choose to constrain CO emissions with the MOPITT surface product for our illustration. Among the different MOPITTv8 products, we choose to work with the multispectral MOPITTv8-NIR-TIR one, as it provides the highest number of observations, with a good evaluation against in situ data from NOAA stations [Deeter et al., 2019]. The MOPITTv8-NIR-TIR surface concentrations are sub-sampled into "super-observations" in order to reduce the effect of correlated errors between neighboring observations in the inversion system*:* we selected the median of each subset of OMI data within each 0.5°×0.5° grid-cell and each physical time step (about 5-10 minutes). After this screening, 1587 "super-observations" remain in the 1-day inversion (from 10667 raw observations). These super-observations are provided to PYVAR-CHIMERE as constraints **y**, and treated as described in Section 3.4. Any other pre-treatment of the data (e.g., no screening or different subsampling, etc) could have been chosen. It is important to note that the potential of MOPITT to provide information at a high temporal resolution, up to the daily scale, is hampered by the cloud coverage (see the blanks in Figure 5b).

The observational constraint on NO_2 emissions comes from the OMI QA4ECV tropospheric columns [Muller et al., 2016; Boersma et al., 2016, Boersma et al., 2017]. The Ozone Monitoring Instrument (OMI), a near-UV/Visible nadir solar backscatter spectrometer, was launched onboard EOS Aura in July 2004. It has been flying on a 705 km sun-synchronous orbit that crosses the Equator at 13:30 LT. Our data selection follows the criteria of the OMI QA4ECV data quality statement. As the spatial resolution of the OMI data is finer than that of the chosen CHIMERE model grid (13x24 km^2 against 0.5°×0.5°, respectively), the OMI tropospheric columns are sub-sampled into "super-observations" (median of the OMI data within the 0.5°×0.5° grid-cell and each physical time step and its corresponding AK).

336

337 ### 4.1.3. Covariance matrices B and R

338 The covariance matrix **B** of the prior errors is defined as diagonal (i.e. only variances are taken into
339 account). Even though total emissions are well known, large uncertainties still affect such emission
340 inventories [Kuenen et al. 2014] at the pixel scale. Consequently, the error standard deviations
341 assigned to the CO and NO_2 prior emissions in the covariance matrix **B** are set at 100%. The variance
342 of the individual observation errors in **R** is defined as the quadratic sum of the measurement error
343 reported in the MOPITT and the OMI data sets, and of the CTM errors (including transport errors
344 and representativity errors) set to 20% of the retrieval values. The representativity errors could have
345 been reduced with the choice of a finer CTM resolution (e.g., with a resolution closer to the size of
346 the satellite pixel). Error correlations between the super-observations are neglected, so that the
347 covariance matrix **R** of the observation errors is diagonal.

348

4.2. Inversion of CO emissions

349 Large discrepancies are found between the MOPITT CO observations and the prior simulation of
350 their equivalents by CHIMERE over Europe (Figure 5). These discrepancies might be explained by
351 an underestimation in the BU inventory due to a general trend in emissions (if the underestimation
352 persists throughout the year) or to an underestimation regarding particular activity sectors or the time
353 profiles at given scales (daily, monthly). This can also be explained by uncertainties from the satellite
354 data or from the CTM (e.g., atmospheric production, chemistry with OH).
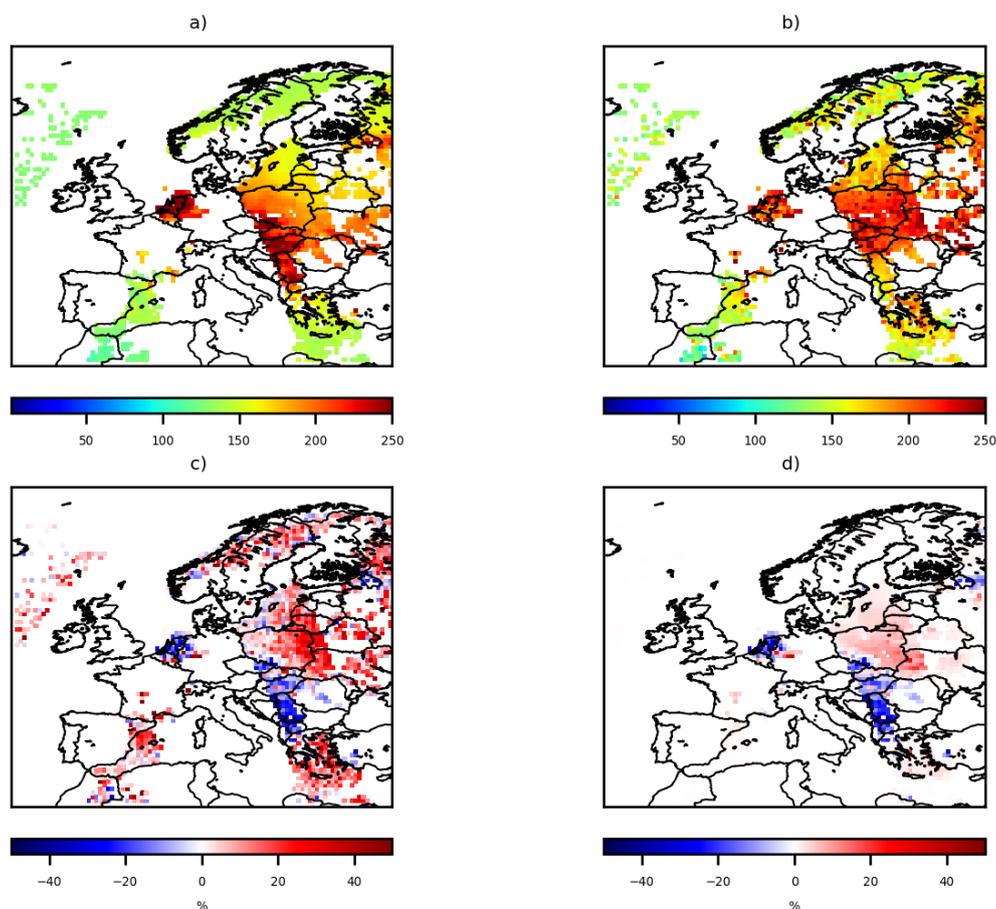
Figure 5. *CO collocated surface concentrations a) simulated by CHIMERE using the prior TNO emissions and b) observed by MOPITTv8-NIR-TIR in ppbv, c) relative differences between the MOPITT observations and the CHIMERE simulated concentrations using the prior TNO emissions, and d) relative differences between the CHIMERE simulated concentrations using the posterior emissions and the CHIMERE simulated concentrations using the prior TNO emissions, in %, at the $0.5° \times 0.5°$ grid-cell resolution, over Europe for the 7th, March 2015.*

356   About 10 iterations are needed to reduce the norm of the gradient of *J* by 90% with the minimization
357   algorithm M1QN3 and obtain the increments i.e. the corrections provided by the inversion. The prior
358   CO emissions over Europe on the 7th, March 2015 and their increments are shown in Figure 6. As
359   expected from the underestimation of the prior surface concentrations in Figure 5, local increments
360   may be significant, reaching more than +50%. The posterior emissions and their uncertainties will
361   have to be evaluated and may bring hints to the cause of the discrepancies. The analyzed

362 concentrations in Figure 5d are the concentrations simulated by CHIMERE with the posterior fluxes:

363 as expected, the optimization of the fluxes improves the fit of the simulated concentrations to the

364 observations.
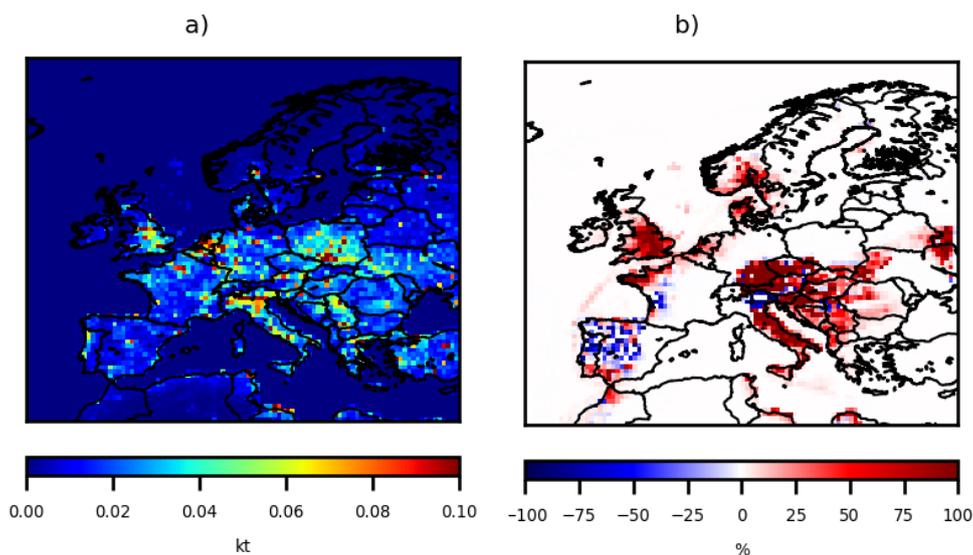
365

366 **Figure 6.** *a) TNO CO anthropogenic prior emissions, in ktCO/grid-cell and b) increments provided*

367 *by the inversion with constraints from MOPITTv8-NIR-TIR for the 7th, March 2015, in %. Note that*

368 *part of Figure 6b presents blanks, as there is no observation to constrain the fluxes (see Figure 5).*

369

4.3. Inversion of NO$_2$ emissions

Large discrepancies are found between the OMI NO$_2$ super-observations and the prior simulation of

their equivalents by PYVAR-CHIMERE (Figure 7). Over Europe, the prior simulation strongly

underestimates the tropospheric columns, and particularly over Po Valley.
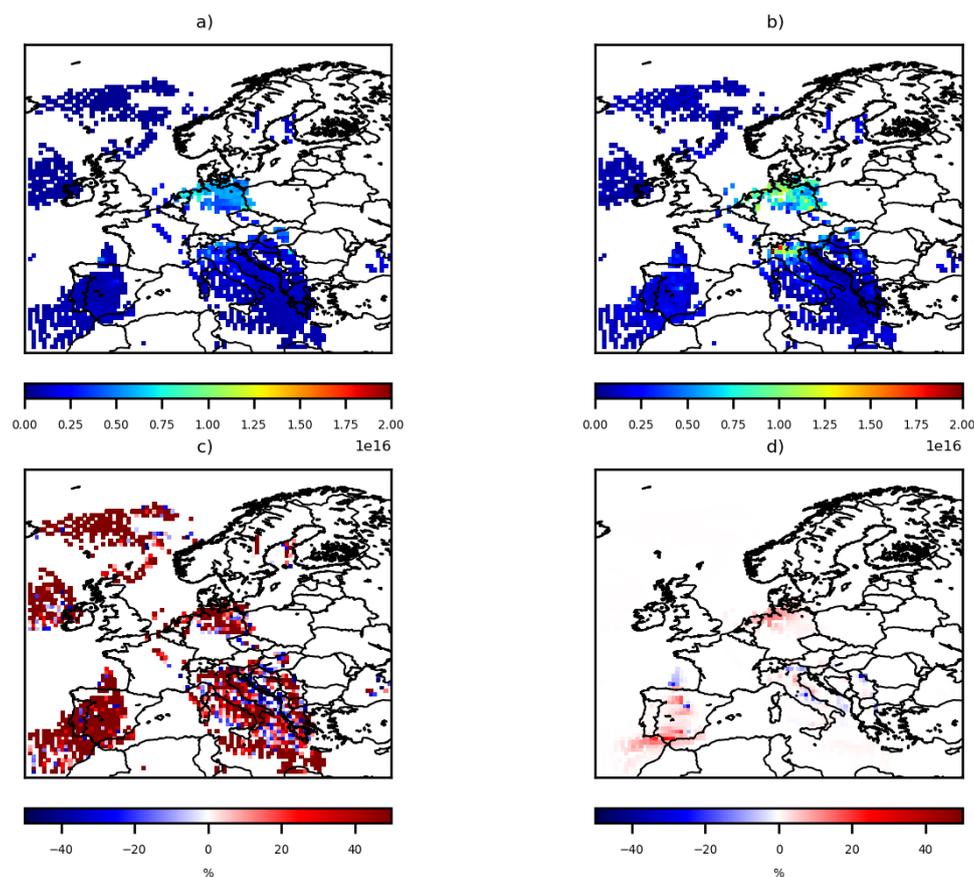
Figure 7. *NO₂ collocated tropospheric columns a) simulated by CHIMERE using the prior TNO emissions, b) observed by OMI, in 1e16 molec.cm⁻², c) relative differences between the OMI observations and the CHIMERE simulated tropospheric columns using the prior TNO emissions, and d) relative differences between the CHIMERE simulated tropospheric columns using the posterior emissions and the CHIMERE simulated tropospheric columns using the prior TNO emissions, in %, at the 0.5°x0.5° grid-cell resolution, for the 19ᵗʰ February 2015, over Europe.*

370   The prior NO₂ emissions and the increments obtained after inversion over Europe for the 19ᵗʰ,

371   February 2015 are shown in Figure 8. As expected from the underestimation of the prior tropospheric

372   columns in Figure 7, local increments may be large, for example over industrial areas (e.g., over the

373   Po Valley) and over large cities (e.g, Madrid), with increments of more than +50% (Figure 8). The

374   analyzed NO₂ tropospheric columns in Figure 5c are the columns simulated by CHIMERE with the

375   NO₂ posterior fluxes: as expected, the optimization of the NO₂ fluxes has only a small impact on the

376   differences between the simulated and observed NO₂ columns. NOₓ emissions are speciated as

377   9.2 % of NO2, 0.8 % of HONO, and 90 % of NO [Menut et al., 2013; Liu et al., 2018], following the

378   Generation of European Emission Data for Episodes (GENEMIS) recommendations [Friedrich, 2000;

379   Kurtenbach et al., 2001; Aumont et al., 2003]. Consequently, the NO_2 fluxes contribute only to about

380   10% to the NO_2 tropospheric column. Further work will be done to simultaneously optimize NO and

381   NO_2 fluxes, which together contribute to more than 99% to the NO_2 tropospheric column.
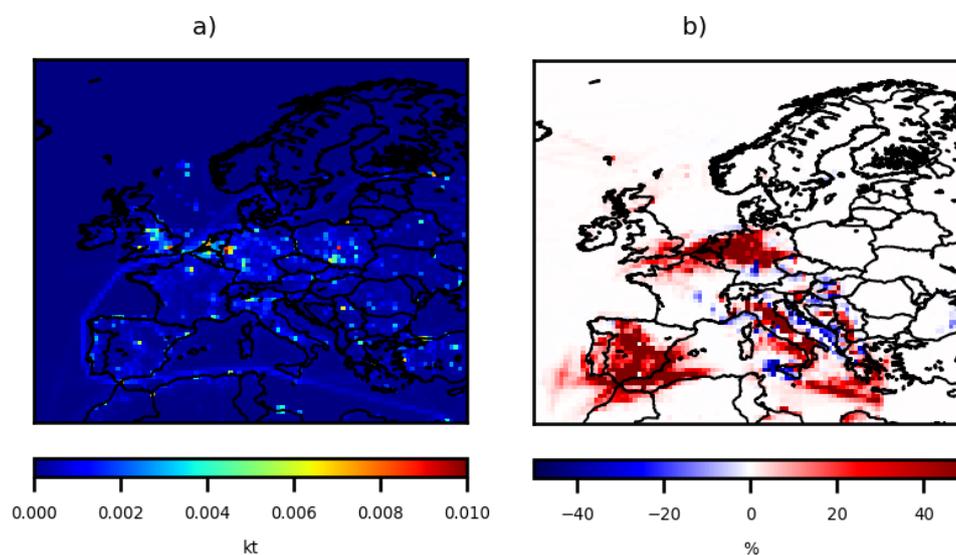
Figure 8. *a) TNO NO_2 anthropogenic prior emissions, in ktNO_2/grid-cell and b) increments provided by the inversion with constraints from OMI for the 19th, February 2015, in %. The configuration of the inversion is detailed in Table 1.*

382   **5. Conclusion/Discussion**

383   This paper presents the Bayesian variational inverse system PYVAR-CHIMERE, which has been

384   adapted to the inversion of reactive species such as CO and NO_2, taking advantage of the previous

385   developments for long-lived species such as CO_2 [Broquet et al., 2011] and CH_4 [Pison et al., 2018].

386   We show the potential of PYVAR-CHIMERE, with inversions for CO and NO_2 illustrated over

387   Europe for an example day. PYVAR-CHIMERE will be used to infer CO and NO_x emissions over

388   long periods, e.g. first for a whole season or year and then for the recent decade 2005-2015 in the

389   framework of the H2020 VERIFY project over Europe, and in the framework of the ANR PolEASIA

390   over China, to quantify their trend and their spatio-temporal variability.

391

392   The PYVAR-CHIMERE system can handle any large number of both control parameters and

393   observations. It will be able to cope with the dramatic increase in the number of data in the near future

394 with, for example, the high-resolution imaging (pixel of 7x3.5 km^2) of the new Sentinel-

395 5P/TROPOMI program, launched in October 2017. These new space missions with high-resolution

396 imaging have indeed the ambition to monitor atmospheric chemical composition for the

397 quantification of anthropogenic emissions. Moreover, a step forward in the joint assimilation of co-

398 emitted pollutants will soon be possible with the PYVAR-CHIMERE system and the availability of

399 TROPOMI co-localized images of NO$_2$ and CO for example. This should improve the consistency of

400 the inversion results and can be used to inform inventory compilers, and subsequently improve

401 emission inventories. Moreover, this development will help in further understanding of air quality

402 problems and help address air quality related emissions at the national to subnational scales.

403

404 **Author Contribution**

405 All authors have contributed to the manuscript writing (main authors: AFC, GB, IP and GD) and to

406 the development of the present version of the PYVAR-CHIMERE system (main developer: IP). IP

407 and GD have parallelized the adjoint version from Menut et al., [2000], Menut et al., [2003] and Pison

408 et al., [2007]. IP has complemented the adjoint of new parameterizations since the CHIMERE release

409 in 2011 and the tangent-linear model.

410

411 **Code and Data Availability**

412 OMI QA4ECV NO$_2$ product can be found here: http://temis.nl/qa4ecv/no2.html.

413 MOPITTv8-NIR-TIR CO product can be found here: ftp://l5ftl01.larc.nasa.gov/MOPITT/

414 The CHIMERE code is available here: www.lmd.polytechnique.fr/chimere/.

415

416 The associated documentation of PYVAR-CHIMERE is available on the website

417 https://pyvar.lsce.ipsl.fr/doku.php/3chimere:headpage. The documentation includes a whole

418 description of PYVAR-CHIMERE and several tutorials on how to run a first PYVAR-CHIMERE

419 simulation or how to run an inversion.

420

421 **Competing interests**

422 The authors declare that they have no conflict of interest.

423

424 **Acknowledgements**

425 We acknowledge L. Menut and C. Schmechtig for their contributions to the development work on

426 the adjoint code of CHIMERE and its parallelization. We acknowledge the TNO team (H.A. Denier

427 van der Gon, J. Kuenen, S. Dellaert, S. Jonkers, A. Visschedijk, et al.) for providing NO$_x$ and CO

428 emissions over Europe. We also acknowledge the free use of tropospheric NO$_2$ column data from the

429 OMI sensor from http://temis.nl/qa4ecv/no2.html and the free use of CO surface concentrations from

430 the MOPITT sensor from ftp://l5ftl01.larc.nasa.gov/MOPITT/. For this study, A. Fortems-Cheiney

431 was funded by the FrenchSpace Agency-Centre National d'Etudes Spatiales CNES and by the H2020

432 VERIFY project, funded by the European Commission Horizon 2020 research and innovation

433 programme, under agreement number 776810. L. Costantino was funded by the PolEASIA ANR

434 project under the allocation ANR-15-CE04-0005.This work was granted access to the HPC resources

435 of TGCC under the allocation A0050107232made by GENCI. Finally, we wish to thank F. Marabelle

436 (LSCE) and his team for computer support.

437

438 **References**

439

440   Aumont, B., Chervier, F., and Laval, S.: Contribution of HONO sources to the
441   NOx/HOx/O3chemistry in the polluted boundary layer, Atmos. Environ., 37, 487–498, 2003.

442

443   Belikov, D. A., Maksyutov, S., Yaremchuk, A., Ganshin, A., Kaminski, T., Blessing, S.,
444   Sasakawa, M., Gomez-Pelaez, A. J., and Starchenko, A.: Adjoint of the global Eulerian–Lagrangian
445   coupled atmospheric transport model (A-GELCA v1.0): development and validation, Geosci. Model
446   Dev., 9, 749-764, https://doi.org/10.5194/gmd-9-749-2016, 2016.

447

448   Boersma, K. F., Vinken, G. C. M., and Eskes, H. J.: Representativeness errors in comparing
449   chemistry transport and chemistry climate models with satellite UV–Vis tropospheric column
450   retrievals, Geosci. Model Dev., 9, 875-898, https://doi.org/10.5194/gmd-9-875-2016, 2016.

451

452   Boersma, K. F., Eskes, H., Richter, A., De Smedt, I., Lorente, A., Beirle, S., Van Geffen, J.,
453   Peters, E., Van Roozendael, M. and Wagner, T.: QA4ECV NO_2 tropospheric and stratospheric
454   vertical column data from OMI (Version 1.1) [Data set], Royal Netherlands Meteorological Institute
455   (KNMI), http://doi.org/10.21944/qa4ecv-no2-omi-v1.1, 2017.

456

457   Bousquet, P., P. Ciais, P. Peylin, M. Ramonet, and P. Monfray: Inverse modeling of annual
458   atmospheric CO_2 sources and sinks: 1. Method and control inversion, *J. Geophys. Res*., 104(D21),
459   26,161 – 26,178, doi:10.1029/1999JD900342, 1999.

460

461   Broquet, G., Chevallier, F., Rayner, P., Aulagnier, C., Pison, I., Ramonet, M., Schmidt, M.,
462   Vermeulen, A. T., and Ciais, P.: A European summertime CO_2 biogenic flux inversion at mesoscale
463   from continuous in situ mixing ratio measurements, *J. Geophys. Res*., 116, D23303, doi:
464   10.1029/2011JD016202, 2011.

465

466   Chevallier, F., M. Fisher, P. Peylin, S. Serrar, P. Bousquet, F.-M. Bréon, A. Chédin, and P.
467   Ciais: Inferring CO_2 sources and sinks from satellite observations: method and application to TOVS
468   data, *J. Geophys. Res*., 110, D24309, doi:10.1029/2005JD006390, 2005.

469

470   Chevallier, F., et al: CO_2 surface fluxes at grid point scale estimated from a global 21 year
471   reanalysis of atmospheric measurements, J. Geophys. Res., 115, D21307,
472   doi:10.1029/2010JD013887, 2010.

473

474   Deeter, M. N., Edwards, D. P., Francis, G. L., Gille, J. C., Mao, D., Martinez-Alonso, S.,
475   Worden, H. M., Ziskin, D., and Andreae, M. O.: Radiance-based Retrieval Bias Mitigation for the
476   MOPITT Instrument: The Version 8 Product, Atmos. Meas. Tech. Discuss.,
477   https://doi.org/10.5194/amt-2019-41, in review, 2019.

478

479   Dellaert, S., Kuenen, J., Denier van der Gon, H., Jonkers, S. and Visschedijk, A.: First high
480   resolution emission data 2005-2015, Deliverable D2.1 in the framework of the VERIFY H2020
481   project, 2018.

482

483   Derognat, C., Beekmann, M., Baeumle, M., Martin, D., and Schmidt, H.: Effect of biogenic
484   volatile organic compound emissions on tropospheric chemistry during the atmospheric pollution
485   over the paris area (ESQUIF) campaign in the ile-de-france region, Journal of Geophysical Research-
486   Atmospheres, 108 (D17), 2003.

487

488   Ding, J., Miyazaki, K., van der A, R. J., Mijling, B., Kurokawa, J.-I., Cho, S., Janssens-
489   Maenhout, G., Zhang, Q., Liu, F., and Levelt, P. F.: Intercomparison of NO_x emission inventories

490   over East Asia, *Atmos. Chem. Phys.*, 17, 10125-10141, https://doi.org/10.5194/acp-17-10125-2017,
491   2017.

493   EEA,   Air   quality   in   Europe   -   2018   report,   12/2018,
494   https://www.eea.europa.eu/publications/air-quality-in-europe-2018.

496   Elbern, H., Strunk, A., Schmidt, H., and Talagrand, O.: Emission rate and chemical state
497   estimation by 4-dimensional variational inversion, Atmos. Chem. Phys., 7, 3749-3769,
498   https://doi.org/10.5194/acp-7-3749-2007, 2007.

500   EMEP/EEA air pollutant emission inventory guidebook, 2016.

502   de Foy, B., Lu. Z. and Streets, D.G.: Satellite NO_2 retrievals suggest China has exceeded its
503   NOx reduction goals from the twelfth Five-Year Plan, *Nature Scientific Reports*, 6:35912, 2016.

505   Friedrich, R.: GENEMIS: Generation of European Emission Datafor Episodes, in: Transport
506   and Chemical Transformation of Pollutants in the Troposphere, edited by: Borrell, P. and Borrell,P.,
507   Vol. 1 of Transport and Chemical Transformation of Pollutants in the Troposphere, 375–386,
508   Springer Berlin Heidelberg, https://doi.org/10.1007/978-3-642-59718-3 18, 2000.

510   Gilbert, J., and C. Lemaréchal (1989), Some numerical experiments with variable storage
511   quasi Newton algorithms,Math. Program., 45, 407–435.

513   Hein, R., et coll.: An inverse modeling approach to investigate the global atmospheric methane
514   cycle, *Global. Biogeochem.Cycles*, 11, 43-76, 1997.

516   Hooghiemstra, P. B., Krol, M. C., Bergamaschi, P., de Laat, A. T. J., van der Werf, G. R.,
517   Novelli, P.C., Deeter, M. N., Aben, I., and Rockmann, T.: Comparing optimized CO emission
518   estimates usingMOPITT or NOAA surface network observations, *J. Geophys. Res.*, 117,
519   D06309,doi:10.1029/2011JD017043, 2012.

521   Konovalov, I. B. et coll.: Inverse modelling of the spatial distribution of NO emissions on a
522   continental scale using satellite data, *Atmos. Chem. Phys.*, 6, 1747-1770, doi:10.5194/acp-6-1747-
523   2006, 2006.

525   Konovalov, I. B., Beekmann, M., Burrows, J. P., and Richter, A.: Satellite measurement based
526   estimates of decadal changes in European nitrogen oxides emissions, *Atmos. Chem. Phys.*, 8, 2623-
527   2641, doi:10.5194/acp-8-2623-2008, 2008.

529   Konovalov, I. B., Beekmann, M., Richter, A., Burrows, J. P., and Hilboll, A.: Multi-annual
530   changes of NO_x emissions in megacity regions: nonlinear trend analysis of satellite measurement
531   based estimates, *Atmos. Chem. Phys.*, 10, 8481-8498, doi:10.5194/acp-10-8481-2010, 2010.

533   Koohkan, M. R., Bocquet, M., Roustan, Y., Kim, Y., and Seigneur, C.: Estimation of volatile
534   organic compound emissions for Europe using data assimilation, *Atmos. Chem. Phys.*, 13, 5887-5905,
535   https://doi.org/10.5194/acp-13-5887-2013, 2013.

537   Kuenen, J. J. P., Visschedijk, A. J. H., Jozwicka, M., and Denier van der Gon, H. A. C.: TNO-
538   MACC_II emission inventory; a multi-year (2003–2009) consistent high-resolution European
539   emission inventory for air quality modelling, Atmos. Chem. Phys., 14, 10963-10976,
540   https://doi.org/10.5194/acp-14-10963-2014, 2014.
541

542   Kurokawa, J., Ohara, T., Morikawa, T., Hanayama, S., Janssens-Maenhout, G., Fukui, T.,
543 Kawashima, K., and Akimoto, H.: Emissions of air pollutants and greenhouse gases over Asian
544 regions during 2000–2008: Regional Emission inventory in ASia (REAS) version 2, *Atmos. Chem.*
545 *Phys.*, 13, 11019-11058, doi:10.5194/acp-13-11019-2013, 2013.

546

547   Kurtenbach, R., Becker, K. H., Gomes, J. A. G., Kleffmann, J.,Lörzer, J. C., Spittler, M.,
548 Wiesen, P., Ackermann, R., Geyer, A.,and Platt, U.: Investigations of emissions and heterogeneous
549 for-mation of HONO in a road traffic tunnel, Atmos. Environ., 35,3385–3394, 2001.

550

551   Lelieveld, J., Klingmüller, K., Pozzer, A., Pöschl, U., Fnais, M., Daiber, A., Münzel, T.;
552 Cardiovascular disease burden from ambient air pollution in Europe reassessed using novel hazard
553 ratio functions, *European Heart Journal*, , ehz135, https://doi.org/10.1093/eurheartj/ehz135, 2019.

554   Lin, J.-T., McElroy, M. B., and Boersma, K. F.: Constraint of anthropogenic NO_x emissions
555 in China from different sectors: a new methodology using multiple satellite retrievals, *Atmos. Chem.*
556 *Phys.*, 10, 63-78, doi:10.5194/acp-10-63-2010, 2010.

557

558   Liu, F., van der A, R. J., Eskes, H., Ding, J., and Mijling, B.: Evaluation of modeling NO_2
559 concentrations driven by satellite-derived and bottom-up emission inventories using in situ
560 measurements over China, Atmos. Chem. Phys., 18, 4171-4186, https://doi.org/10.5194/acp-18-
561 4171-2018, 2018.

562

563   Locatelli, R., Bousquet, P., Saunois, M., Chevallier, F., and Cressot, C.: Sensitivity of the
564 recent methane budget to LMDz sub-grid-scale physical parameterizations, Atmos. Chem. Phys., 15,
565 9765-9780, https://doi.org/10.5194/acp-15-9765-2015, 2015.

566

567   Mailler S., L. Menut, D. Khvorostyanov, M. Valari, F. Couvidat, G. Siour, S. Turquety, R.
568 Briant, P. Tuccella, B. Bessagnet, A. Colette, L. Letinois, and F. Meleux, CHIMERE-2017: from
569 urban to hemispheric chemistry-transport modeling , *Geosci. Model Dev.*, 10, 2397-2423,
570 https://doi.org/10.5194/gmd-10-2397-2017, 2017.

571

572   Menut, L., R. Vautard, M. Beekmann, and C. Honoré: Sensitivity of photochemical pollution
573 using the adjoint of a simplified chemistry-transport model, *J. Geophys. Res.*, 105, 15,379–15,402,
574 2000.

575

576   Menut L.: Adjoint modelling for atmospheric pollution processes sensitivity at regional scale
577 during the ESQUIF IOP2, Journal of Geophysical Research - Atmospheres, 108, D17,
578 https://doi.org/10.1029/2002JD002549, 2003.

579

580   Menut, L., Goussebaile, A., Bessagnet, B., Khvorostiyanov, D., and Ung, A.: Impact of
581 realistic hourly emissions profiles on air pollutants concentrations modelled with CHIMERE,
582 Atmospheric Envionment, 49, 233–244, doi:10.1016/j.atmosenv.2011.11.057, 2012.

583

584   Menut, L., Bessagnet, B., Khvorostyanov, D., Beekmann, M., Blond, N., Colette, A., Coll, I.,
585 Curci, G., Foret, G., Hodzic, A., Mailler, S., Meleux, F., Monge, J.-L., Pison, I., Siour, G.,Turquety,
586 S., Valari, M., Vautard, R., and Vivanco, M. G.: CHIMERE 2013: a model for regional atmospheric
587 composition modelling, *Geosci. Model Dev.*, 6, 981–1028, doi:10.5194/gmd-6-981-2013, 2013.

588

589   Mijling, B., and R. J. van der A: Using daily satellite observations to estimate emissions of
590 short-lived air pollutants on a mesoscopic scale, *J. Geophys. Res.*, 117, D17302,
591 doi:10.1029/2012JD017817, 2012.

592

593   Mijling, B., et al., Regional nitrogen oxides emission trends in East Asia observed from space,
594   *Atmos. Chem. Phys.*, 3, 12003, 2013.

596   Muller, J.-P., Kharbouche, S., Gobron, N., Scanlon, T., Govaerts, Y., Danne, O., Schultz, J.,
597   Lattanzio, A., Peters, E., De Smedt, I., Beirle, S., Lorente, A., Coheur, P. F., George, M., Wagner, T.,
598   Hilboll, A., Richter, A., Van Roozendael, M., and Boersma, K. F.: Recommendations (scientific) on
599   best practices for retrievals for Land and Atmosphere ECVs (QA4ECV Deliverable 4.2 version 1.0),
600   186 pp., available at: http://www.qa4ecv.eu/sites/default/ files/D4.2.pdf (last access: 12 April 2018),
601   2016.

603   Owens, R. G. and Hewson, T.: ECMWF Forecast User Guide, Reading,
604   https://doi.org/10.21957/m1cs7h,https://software.ecmwf.int/wiki/display/FUG/Forecast+User+Guid
605   e, 2018.

607   Pison, I., Menut, L., and Bergametti, G.: Inverse modeling of surface NOx anthropogenic
608   emission fluxes in the Paris area during the ESQUIF campaign, *J. Geophys. Res. Atmos.*, 112,
609   D24302, doi:10,1029/2007JD008871, 2007.

611   Pison, I., Bousquet, P., Chevallier, F., Szopa, S., and Hauglustaine, D.: Multi-species
612   inversion of CH_4, CO and H_2 emissions from surface measurements, *Atmospheric Chemistry and*
613   *Physics*, 9, 5281-5297, 2009.

615   Pison, I., A. Berchet, M. Saunois, . How a European network may constrain methane
616   emissions at the French national scale. *Atmospheric Chemistry and Physics*, 2018.

618   Stavrakou, T. and J.-F. Müller: Grid-based versus big region approach for inverting CO
619   emissions using Measurement of Pollution in the Troposphere (MOPITT) data, *Journal of*
620   *Geophysical Research: Atmospheres*,111, D15, 2006.

622   Stavrakou, T., Muller, J.-F., Boersma, K. F., De Smedt, I., and van der A, R. J.: Assessing the
623   distribution and growthrates of NOx emission sources by inverting a 10-year record of NO_2 satellite
624   columns, *Geophys. Res. Lett.*, 35, 1–5, doi:10.1029/2008GL033521, 2008.

626   Szopa, S., Foret, G., Menut, L., and Cozic, A.: Impact of large scale circulation on European
627   summer surface ozone: consequences for modeling, *Atmospheric Environment*, 43, 1189–
628   1195,doi:10.1016/j.atmosenv.2008.10.039, 2008.

630   Talagrand, O. : Assimilation of observations : an introduction, J. Met. Soc., Japan, 75, 191-
631   209, 1997.

633   van der A, R. J., Mijling, B., Ding, J., Koukouli, M. E., Liu, F., Li, Q., Mao, H., and Theys,
634   N.: Cleaning up the air: Effectiveness of air quality policy for SO_2 and NO_x emissions in China,
635   *Atmos. Chem. Phys.*, 17, 1775-1789, 2017.

637   Yin, Y., Chevallier, F., Ciais, P., Broquet, G., A. Fortems-Cheiney, Pison, I. and Saunois, M:
638   Decadal trends in global CO emissions as seen by MOPITT, *Atmos. Chem. Phys.*, 15, 13433-13451,
639   2015.

641   Yumimoto, K. and Uno, I.: Adjoint inverse modeling of CO emissions over Eastern Asia using
642   four-dimensional variational data assimilation, Atmospheric Environment, 40, 35, 6836-6845, DOI:
643   10.1016/j.atmosenv.2006.05.042, 2006.

644

645
646   WHO World Health Organization: Ambient Air Pollution: a global assessment of exposure
647 and burden of disease, 2016.
648
649   Zheng, B., Chevallier, F., Yin, Y., Ciais, P., Fortems-Cheiney, A., Deeter, M. N., Parker, R.
650 J., Wang, Y., Worden, H. M., and Zhao, Y.: Global atmospheric carbon monoxide budget 2000–2017
651 inferred from multi-species atmospheric inversions, Earth Syst. Sci. Data Discuss.,
652 https://doi.org/10.5194/essd-2019-61, in review, 2019.
653
654
655
656
657
658